



Published in final edited form as:

Cell Rep. 2022 April 26; 39(4): 110666. doi:10.1016/j.celrep.2022.110666.

Convergent extension requires adhesion-dependent biomechanical integration of cell crawling and junction contraction

Shinuo Weng¹, Robert J. Huebner¹, John B. Wallingford^{1,2,*}

¹Department of Molecular Biosciences, Patterson Labs, The University of Texas at Austin, 2401 Speedway, Austin, TX 78712, USA

²Lead contact

SUMMARY

Convergent extension (CE) is an evolutionarily conserved collective cell movement that elongates several organ systems during development. Studies have revealed two distinct cellular mechanisms, one based on cell crawling and the other on junction contraction. Whether these two behaviors collaborate is unclear. Here, using live-cell imaging, we show that crawling and contraction act both independently and jointly but that CE is more effective when they are integrated via mechano-reciprocity. We thus developed a computational model considering both crawling and contraction. This model recapitulates the biomechanical efficacy of integrating the two modes and further clarifies how the two modes and their integration are influenced by cell adhesion. Finally, we use these insights to understand the function of an understudied catenin, Arvcf, during CE. These data are significant for providing interesting biomechanical and cell biological insights into a fundamental morphogenetic process that is implicated in human neural tube defects and skeletal dysplasias.

Graphical abstract

This is an open access article under the CC BY-NC-ND license (<http://creativecommons.org/licenses/by-nc-nd/4.0/>).

*Correspondence: wallingford@austin.utexas.edu.

AUTHOR CONTRIBUTIONS

S.W. and J.B.W. conceptualized the project, designed and conducted the experiments, performed analysis, developed the model, and wrote the manuscript. R.J.H. assisted in data acquisition and writing of the manuscript. All authors provided revisions and comments.

SUPPLEMENTAL INFORMATION

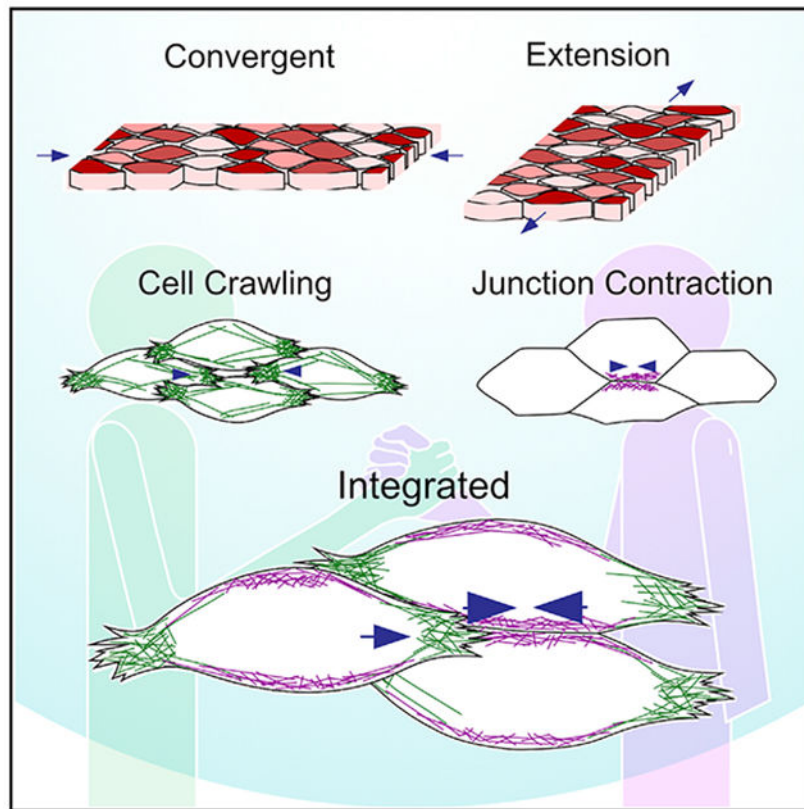
Supplemental information can be found online at <https://doi.org/10.1016/j.celrep.2022.110666>.

DECLARATION OF INTERESTS

The authors declare no competing interests.

SUPPORTING CITATIONS

The following references appear in the supplemental information: Abraham et al. (1999); Petrie et al. (2014); Prass et al. (2006); Truong Quang et al. (2013).



In brief

Cell crawling and junction contraction are thought to be two distinct mechanisms used for elongation by convergent extension during embryonic development. Weng et al. demonstrate that the two modes not only work together but also collaborate for a better efficacy. A computational model is also developed to model this collaboration.

INTRODUCTION

Convergent extension (CE) is a fundamental collective cell movement in which a developing tissue converges along one axis, thereby extending in the orthogonal direction (Figure 1A). CE plays a crucial role in embryogenesis by shaping the body axis during gastrulation and neurulation and by elongating tubular organs during organogenesis (Tada and Heisenberg, 2012; Keller, 2002; Lienkamp et al., 2012). The cell movements of CE are evolutionarily conserved in animals ranging from nematodes and arthropods to vertebrates (Huebner and Wallingford, 2018; Walck-Shannon and Hardin, 2014). Moreover, failure of CE is associated with severe birth defects, including neural tube defects, heart defects, and skeletal dysplasias (Butler and Wallingford, 2017; Wallingford et al., 2013).

Two distinct cellular mechanisms for CE have been described, and they were initially discovered in different cell types. The first was discovered by work on *Xenopus* body axis elongation during gastrulation (Keller and Hardin, 1987; Keller and Tibbetts, 1989; Shih and Keller, 1992). In this case, intercalation of mesenchymal cells is driven by polarized

actin-based protrusions extending from the opposing vertices of mediolateral cells (referred to hereafter as “ML cells”; Figure 1B) (Keller et al., 1992). These protrusions resemble a combination of the sheet-like lamellipodia and spike-like filopodia observed on the leading edge of cultured migrating cells (Devitt et al., 2021), pushing the boundary between neighboring cells and bringing ML cells together (Figure 1B). They also form adhesions with the substrate and with the neighboring cells, thus driving cell intercalation in a manner similar to cell migration (Keller and Sutherland, 2020; Pfister et al., 2016).

The second cellular mechanism was discovered in epithelial cells during *Drosophila* germband extension (Irvine and Wieschaus, 1994). In this case, cell intercalation is achieved via polarized junction remodeling, in which junctions joining anteroposterior neighboring cells (referred to hereafter as “AP cells”) shorten to bring together the two dorsoventral neighboring cells. Actomyosin accumulates on the AP cell interfaces and is activated to provide the contractile force (Zallen and Wieschaus, 2004; Bertet et al., 2004) (Figure 1C). We will refer to these two distinct modes as the “crawling” and “contraction” modes, respectively (Figures 1B and 1C).

The two modes were initially considered as distinct mechanisms that were implemented in either mesenchyme or epithelia (e.g., Lienkamp et al., 2012; Nishimura et al., 2012), cell types that differ significantly in terms of cell-cell adhesion and cell polarity. However, recent evidence suggests that many cell types employ both modes during CE (Huebner and Wallingford, 2018; Shindo, 2018). For example, the two modes were found to work in conjunction in epithelial cells, first in the mouse neural plate, and later in the *Drosophila* germ band (Sun et al., 2017; Williams et al., 2014). In both cases, the crawling mode acts via basolaterally positioned protrusions, while contractions act apically at the epithelial junctions. Interestingly, we previously identified a role for the contraction mode in CE of mesenchymal cells of the *Xenopus* notochord (Shindo and Wallingford, 2014; Shindo et al., 2019), the very cells in which the crawling mode was first defined.

Together, these previous studies suggest that crawling and contraction modes may be integrated in some manner to confer a maximal biomechanical advantage. The nature of such integration is unknown. Here, we used quantitative live-cell microscopy and a computational model to demonstrate that cell crawling and junction contraction act both independently and collaboratively to drive CE during *Xenopus* gastrulation. Furthermore, an interesting modeling approach suggests that fine control of cell adhesion is essential for mechano-reciprocal integration of crawling and contraction, and experimental manipulation of the cadherin-interacting catenin Arvcf *in vivo* validated this prediction. These data provide biomechanical and cell biological insights into a fundamental morphogenetic process implicated in human diseases and have broader impacts on studies of collective cell movement in various contexts.

RESULTS

Crawling and contraction modes of intercalation act both independently and in concert during vertebrate convergent extension

The mesenchymal cells of *Xenopus* gastrula mesoderm are a key paradigm for studies of CE (Keller et al., 2003; Chu et al., 2020), and while both crawling- and contraction-based cell intercalation mechanisms have been explored, how the two are coordinated remains unclear (Huebner and Wallingford, 2018; Shindo, 2018). We therefore sought to simultaneously assess the contributions of crawling and contraction using explants of the *Xenopus* dorsal mesodermal tissue (“Keller” explants).

We therefore used uniform labeling with membrane-BFP to segment cells and to assess cell intercalation and used mosaic labeling for different colors of an actin biosensor (Lifeact-RFP/Lifeact-GFP) to differentiate populations of actin in neighboring cells (Figures 1D–1H and Video S1). In this assay, we could clearly distinguish actin dynamics in ML cell protrusions from cortical actin dynamics in adjacent AP cells (Figures 1I–1K and S1A–S1C). When observed in kymographs, both the ML- and AP-associated actin dynamics were pulsatile and highly heterogeneous, as expected (Figures 1L and 1M, S1D and S1E) (Shindo and Wallingford, 2014; Shindo et al., 2019; Kim and Davidson, 2011; Pfister et al., 2016). These kymographs further suggested that both ML and AP actin dynamics were concentrated in regions near tricellular vertices (Figures 1L and 1M, “tCR”), while AP pulses outside these regions appeared less frequent and less pronounced (Figure 1M, “Mid”; See STAR Methods for detailed definition of tCR and Mid regions).

We then quantified the contributions of crawling and contraction to cell intercalation. Details are presented in the STAR Methods and in Figure S2, but we will summarize here: (1) We quantified cell intercalation by measuring the displacement of tricellular vertices connecting AP and ML cells (Figure 1I). (2) We quantified crawling using ML actin intensity as a proxy (Figure 1J). (3) We quantified contraction using AP actin intensity as a proxy (Shindo and Wallingford, 2014; Shindo et al., 2019), treating AP actin dynamics in the tCR and Mid regions independently (Figure 1K). (4) For both displacement and actin dynamics, we quantified each tricellular region separately, as these are known to behave independently in diverse models of intercalation (Figure S3A) (Vanderleest et al., 2018; Huebner et al., 2021; Cavanaugh et al., 2022). In bulk analysis, intercalation correlated little with crawling, tCR contraction, or mid contraction (Figures S3B–S3D). By contrast, we observed a much stronger correlation between crawling and tCR contraction at each tCR (Figure S3E), suggesting the possibility of cooperative action.

We considered that crawling and contraction mechanisms could either “take turns” or work together or both. To explore these possibilities, we took advantage of the pulsatile nature of both cell movement and actin dynamics during CE (Video S2). We first used individual peaks in intercalation velocity curves over time to identify single intercalation “steps” (Figure 2A, left). Then, for each step, we searched for cross-correlated peaks in ML and AP actin intensity within the 40-s window preceding the velocity peak (Figure 2A, right). This method allowed us to unambiguously associate each step of cell intercalation movement with crawling- and/or contraction-related actin dynamics (e.g., Figure S4A).

In our data, we identified intercalation steps associated exclusively with ML cell crawling (i.e., correlated with a crawling peak in ML actin intensity; Figure 2B; Video S3) as well as steps associated exclusively with contraction (i.e., correlated with a contraction peak in AP actin intensity; Figure 2C and Video S3). In addition, we identified steps associated with peaks in both ML and AP actin intensity (Figures 2D, 2E and Video S3). These “concurrent” intercalation steps included cases in which a crawling peak precedes a contraction peak (Figure 2D and Video S3) and a similar number of cases in which a contraction peak precedes a crawling peak (Figure 2E and Video S3). We note here that we also observed a small number of intercalation steps associated exclusively with non-tCR contraction from the middle portion of an AP interface (Figure S4B and Video S3) as well as steps for which no associated crawling or contraction peak could be identified (Figure S4C, “Others”). Since the vast majority of intercalation can be explained by ML crawling or tCR contraction or both (Figure S4C), steps in these latter two categories were removed from further analysis.

We found that roughly one-third of steps were associated purely with crawling, another third with contraction, and the final third with both concurrently (Figure 2F, left). Intercalation steps are known to be highly heterogeneous, so it was notable that when we considered the time, rather than the number of steps, we again found an equal distribution of crawling, contraction, and concurrent steps (Figure 2F, middle). By contrast, when we considered actual displacement for cell intercalation, we found that concurrent steps accounted for far more than one-third of the total intercalation displacement moved by tricellular vertices (Figure 2F, right). Together, these data suggest that crawling and contraction can be simultaneously integrated to produce more effective cell movement than can either mode acting alone.

Concurrent crawling and contraction improve the efficacy of cell intercalation

To further define crawling-only, contraction-only, and concurrent intercalation steps, we quantified several additional metrics. We found that the significantly higher displacement for concurrent steps (Figure 3A) was related to an increase both in the duration of steps and the velocity of vertex movement (Figures 3B and 3C). Moreover, we noted that some steps involved multiple, successively correlated crawling and contraction peaks (Figure 3D), suggesting an iterative integration of crawling and contraction. We reasoned that if concurrent crawling and contraction provided better efficacy, then multiple concurrent crawling and contraction pulses should be more productive. This was indeed the case, as intercalation accompanied by three or more concurrent crawling and contraction peaks exhibited significantly more displacement and a significantly longer duration than did those accompanied by only two concurrent peaks (Figures 3E and 3F). Thus, concurrent crawling and contraction produces more effective movement by making each intercalation step both longer lasting and faster than crawling-only or contraction-only steps.

Concurrent crawling and contraction amplify actin assembly of both mechanisms

We next sought to understand how concurrent crawling and contraction produced more effective intercalation than does either mode alone. One possibility is biomechanical feedback of actomyosin networks. For example, previous studies in *Drosophila* suggest that tension generated by actomyosin contraction in one cell can stimulate actomyosin

contraction in an adherent neighboring cell (e.g., Martin et al., 2010; Fernandez-Gonzalez et al., 2009). To ask if a similar mechanism was at work here, we first compared contraction-related AP actin dynamics during contraction-only steps with that of AP actin during concurrent steps (Figure 4A). Strikingly, both the peak intensity and the duration of AP actin pulses associated with concurrent steps were significantly amplified compared to contraction-only steps (Figures 4B and 4C).

We performed a complementary analysis of crawling-related ML actin dynamics (Figure 4D), and we observed a similar trend; the peak intensity and duration of crawling protrusions were amplified in concurrent steps relative to crawling-only steps (Figures 4E and 4F). Thus, concurrent execution of crawling and contraction has a synergistic effect, enhancing actin assembly of both modes. This result suggests that the concurrent steps are, in fact, integrated and that mechano-reciprocity amplifies forces when crawling and contraction occur concurrently (schematized in Figure 4G).

A vertex model recapitulates integrated crawling- and contraction-based convergent extension

Theoretical modeling is a crucial tool in studies of morphogenesis, as it allows manipulation of attributes that may be difficult or impossible to manipulate experimentally, and several modeling studies have been used to explore the mechanisms of CE (e.g., Merkel and Manning, 2017; Alt et al., 2017; Fletcher et al., 2017). However, the vertex models commonly employed for such studies are limited, because (1) they generally treat two sides of a cell-cell interface as a single feature; (2) heterogeneity along a single cell-cell interface is generally ignored; and (3) they do not independently consider contributions from cell crawling and junction contraction (Brodland, 2006; Belmonte et al., 2016; Finegan et al., 2019; Shindo et al., 2019).

To overcome these limitations, we re-envisioned the vertex model of CE. We represented each cell not as a six-vertex hexagon, but instead as a 90-vertex polygon, allowing us to model local events in discrete regions of individual cell-cell interfaces (Figure 5A). Furthermore, cell-cell interfaces *in vivo* are formed of two apposed cell membranes, which are linked by cell-cell adhesion molecules but can behave independently. We therefore modeled junctions between two cells as two independent entities (Figure 5B), while modeling cell adhesion to connect adjacent cells (Figure 5C).

Details of the model are presented in the STAR Methods, but briefly, we invoke three key forces: First, the pushing force for cell crawling was modeled as a defined force profile applied on tricellular vertices (Figure 5D, " F_{craw} "). Second, the contractile force from actomyosin pulses (" M_{pulse} ") for junction contraction was modeled with Hill's muscle model (Mitrossilis et al., 2009) (Figure 5E, " $F_{contract}$ "). Finally, we modeled the force transmitted between neighboring cells via force-dependent cell adhesion at cell interfaces using a catch-slip bond model (Figure 5C, " $F_{adhesion}$ "), which reflects the known role of cadherin adhesion in CE (Brieher and Gumbiner, 1994; Fagotto et al., 2013; Pfister et al., 2016; Huebner et al., 2021). Without loss of generality, this model is dimensionless, but parameters for the key force components were estimated from experimental data, with their relative values in a physiologically relevant range (Table S1).

Critically, our model successfully recapitulated many gross aspects of CE. For example, we first modeled cell intercalation using four-cell models (Figure 5F; Video S4). To reproduce actin dynamics observed *in vivo* (Figures 1L and 1M), medially directed crawling forces (“ F_{crawl} ”) and heterogenous actomyosin pulses along the AP cell interface (“ M_{pulse} ”) were applied at randomized timepoints (Figures S5A and S5B). This configuration consistently produced complete cell intercalation (i.e., “T1 transition”), including shortening of the AP cell interface and formation and elongation of a new AP-directed cell-cell interface (Figure 5F and Video S4). We also demonstrated using our model that contraction from the middle portion of an AP cell interface has limited effect on cell intercalation at tCRs (Figure S5D), consistent with *in vivo* data (Figure S4C).

Moreover, 27-cell clusters in which both medially and laterally directed crawling forces were applied to each cell at equal probability consistently recapitulated not just cell intercalation but also tissue-wide CE (Figure 5G and Video S5). Importantly, cells were able to accomplish multiple rounds of cell intercalation and interdigitated in a regular manner (Figure 5G). Future cell elongation in the ML axis with cell intercalation was also observed, similar to the reported cell shape change *in vivo* (Wilson et al., 1989). Thus, a combination of crawling and contraction in our model can recapitulate cell movements and tissue morphology change observed in vertebrate CE *in vivo*.

Modeling recapitulates biomechanical synergy of crawling/contraction integration

As a further test of our model’s validity, we asked if it could also recapitulate finer-scale behaviors observed *in vivo*. To this end, we used four-cell models to simulate shortening of AP interfaces. We set medially directed crawling forces and AP actomyosin pulses in tCRs to defined time points, so we could distinguish crawling-only or contraction-only steps from steps with concurrent crawling and contraction (Figure 5H). Importantly, we found that across a wide range of parameters for F_{crawl} and M_{pulse} concurrent crawling and contraction in the model elicited significantly greater displacement and mean intercalation velocity (Figures 5I, 5J, S6A, and S6B), similar to the effects observed for concurrent steps *in vivo*.

This finding prompted us to ask if our model also recapitulated the amplification of actin assembly during concurrent steps that we observed *in vivo* (Figure 4). We defined effective protrusion intensity in our model as the integral of protrusion length over time and used it as a proxy for protrusion dynamics (Figure S5E). We reasoned that this is a mechano-responsive measure for a given crawling force, reflecting the interaction between a protrusion and its adjacent cells by considering both protrusion extension and retraction (Figure S5E). We found that when crawling and contraction occurred concurrently, the effective protrusion intensity was significantly higher than when a crawling force was applied alone (Figure 5K). This effect held for a wide range of crawling forces and actomyosin pulses (Figures S6C and S6D). Importantly, this mechano-reciprocity was not explicitly designed in the model, but nonetheless recapitulated that observed *in vivo* (i.e., Figures 4D–4F).

Similarly, our model imposed actomyosin pulses (“ M_{pulse} ”) for contraction, and the corresponding contraction forces (“ $F_{contract}$ ”) can be estimated directly from the Hill’s muscle model (see STAR Methods; example in Figures S5B and S5C). Mechanical forces

are known to promote assembly of actomyosin structures, forming a feedforward loop in several contexts, including CE (Martin et al., 2010; Fernandez-Gonzalez et al., 2009; Uyeda et al., 2011; Zaidel-Bar et al., 2015; Miao and Blankenship, 2020). We therefore used the calculated contraction force as a proxy for actin dynamics at the AP cell cortex. Over a wide range of crawling forces and actomyosin pulses, we observed amplified contraction forces when crawling and contraction occurred concurrently (Figures 5L, S6E, and S6F). Because this is not an explicit feature in the model, it suggests a mechano-reciprocal integration of crawling and contraction similar that observed *in vivo* (i.e., Figures 4A–4C).

Thus, our model recapitulated not only the tissue-scale and cell-scale CE, but also the synergy of crawling/contraction integration for both cell intercalation and enhanced actin assembly. The synergistic effects observed both *in vivo* and *in silico* suggest a mechano-reciprocity between the two distinct populations of actomyosin that drives integration of the crawling and contraction modes of CE.

Modeling provides insight into the role of regulated adhesion in crawling, contraction, and their integration

Our working model for crawling/contraction integration schematized in Figure 4G suggested a strong dependency on cell adhesion for effective integration. Thus, we next examined the effect of cell adhesion by modulating the total adhesion units available, $N_{adhesion}^{tot}$, while maintaining a constant, moderate crawling force, F_{crawl} , and constant moderate actomyosin pulses, M_{pulse} .

Interestingly, when we reduced adhesion by half, we still consistently observed complete cell intercalation in four-cell models (Figure 6A), though it was characterized by enlarged extracellular voids between cells, particularly in tricellular and quad-cellular regions, reflecting the effect of reduced cell adhesion (Figure 6A, insets). More strikingly, when we simulated CE in a 27-cell model with reduced adhesion, tissue-wide CE was substantially reduced, intercellular voids were enlarged, and cell packing was much less regular (Figure 6B).

We then used the modeling approaches outlined earlier (i.e., Figure 5H) to ask how modulation of adhesion impacts different modes of cell intercalation. We found that higher adhesion strongly inhibited crawling-only intercalation while favoring contraction-only intercalation (Figures 6C and 6D, “Low” versus “WT”). It is also notable that these effects plateaued when adhesion strength increased further. Surprisingly, across a wide range of adhesion strength, elevated intercalation with concurrent crawling and contraction was maintained robustly (Figure 6E).

We next examined the impact of adhesion on integrating concurrent crawling and contraction. We found that effective protrusion intensity tended to decrease as adhesion increased (Figure 6F), a result similar to cadherin-mediated contact inhibition of locomotion *in vivo* (Becker et al., 2014). More interestingly, amplification of protrusion intensity during concurrent steps was only observed when adhesion was in the medium-high regimes (Figure 6F). In low-adhesion regimes, protrusion was indeed diminished in concurrent steps compared with crawling-only steps (Figure 6F, “Low”), reflecting the requirement for

adhesion between protrusions and the cortex of another cell to interact. In contrast, there was a pronounced trend for the contraction force to increase with adhesion (Figure 6G), consistent with the thought that anchoring sites are necessary for the actomyosin to generate cortical tension. Interestingly, the synergistic effect on contraction force during concurrent steps was quite robust to changes in adhesion (Figure 6G), suggesting a differential impact of adhesion and the transmitted force on contraction versus crawling.

Multiple functions of the Arvcf catenin are required for normal integration of crawling and contraction

Finally, we considered that this quantitative understanding of the interplay of crawling and contraction during CE might shed light on complex experimental loss-of-function phenotypes. For example, the Arvcf catenin is a C-cadherin/Cdh3-interacting protein that is required for *Xenopus* CE (Fang et al., 2004; Paulson et al., 2000). In a companion paper, we show that loss of Arvcf decreased the tissue-level extension force by cell intercalation, leading to CE defect in embryos (Huebner et al., 2022). The cell biological basis of this phenotype is not known, so we turned to our mosaic labeling approach and our model for insight.

Live imaging of mosaically labeled explants revealed that Arvcf loss (see STAR Methods) did not affect cell shape (Figure 7A), but it did decrease overall intercalation velocity (Figure 7B). Interestingly, analysis of individual intercalation steps revealed that crawling-only and contraction-only steps were not affected (Figure 7C), but in striking contrast, intercalation during concurrent steps was significantly reduced in the absence of Arvcf (Figure 7C, right). This mosaic analysis further revealed that the defect in concurrent steps was associated specifically with a failure to amplify crawling-associated actin dynamics during concurrent steps, contraction-associated actin dynamics remained significantly amplified (Figures S7A–S7D). This result suggested a specific role for Arvcf in the normal synergistic integration of crawling and contraction.

Turning to our model, we first considered that loss of Arvcf elicits a small but significant reduction in cortical cadherin levels, resulting in enlarged gaps between cells (Huebner et al., 2022). Curiously, while reducing adhesion alone in our model could elicit the formation of extracellular gaps (Figures 6A and 6B), it could not recapitulate the specific disruption of concurrent steps that we observed for Arvcf loss *in vivo* (Figures 6C–6E).

This result suggested that Arvcf plays a more complex role, so we performed a broader survey of parameter space in our model. Strikingly, only one set of parameters in the ranges tested here recapitulated the concurrent step-specific defect in intercalation (Figure 7D). These parameters (–25% adhesion [$N_{adhesion}^{tot}$]; –23% crawling [F_{crawl}]; +7% contraction [M_{pulse}]) also recapitulated the defect in amplification of crawling-associated protrusions during concurrent steps (Figure S7E), leaving the amplification of contraction-associated forces unaltered (Figure S7F). Finally, these model parameters also recapitulated the failure of CE (Figure 7E). Thus, our model faithfully modeled *in silico* both fine and gross aspects of the Arvcf knockdown phenotype that we observed *in vivo*.

DISCUSSION

Here, we have combined live imaging and modeling to explore the mechanisms by which two modes of cell motility—protrusive crawling and cortical contraction—collaborate to drive a crucial morphogenetic process in early vertebrate embryos. Our live imaging approach allowed us to independently identify and quantify the actin assembly associated with crawling or contraction (Figures 1, 2, and 3). By doing so, we show that when crawling and contraction occur concurrently during mesenchymal CE in *Xenopus*, actin assembly associated with both mechanisms is amplified (Figure 4). Moreover, this amplification of actin assembly in turn is associated with significantly improved efficacy of cell intercalation. Similar mechanosensitive responses of actomyosin are observed in diverse epithelial cells (e.g., Martin et al., 2010; Fernandez-Gonzalez et al., 2009), so our work here in mesenchymal cells in *Xenopus* suggests that the crawling- and contraction-based intercalation mechanisms in epithelial cells (e.g., Sun et al., 2017; Williams et al., 2014) may be similarly coupled.

In addition, our modeling of CE provides a substantial advance over previous models. It independently captures junction contraction, cell crawling, and cell-cell adhesion, while also treating individual cell cortices independently from one another. The model therefore allows detailed description of both gross tissue movement as well as the diverse underlying subcellular behaviors (Figures 5 and 6). This is crucial, since individual cell-cell junctions during *Xenopus* CE display very local heterogeneities in their mechanical properties (Huebner et al., 2021). Similar local heterogeneity has also been observed during CE in *Drosophila* epithelial cells (Vanderleest et al., 2018) and when junction shortening is artificially induced in cell culture (Cavanaugh et al., 2022). Despite our substantially more complex model, it nonetheless recapitulates both gross and fine characteristics of vertebrate CE observed *in vivo* (Figure 5). Given the model's ability to provide insights into complex phenotypes observed *in vivo* (Figure 7), we feel this model will provide a very useful resource for the community.

Finally, this work also provides insights into the role of cell adhesion during CE. The little-studied Arvcf catenin not only tunes cadherin adhesion, but it also functionally interacts with the small GTPases RhoA and Rac, negatively regulating RhoA function and conversely promoting Rac function (Fang et al., 2004). How these functional interactions relate to cell behaviors is not known, but our data and modeling suggest that Arvcf-mediated Rac activity is necessary for normal ML crawling, while Arvcf-tempering of RhoA activity is needed to restrain AP contraction. In light of previous data on the cell biological roles of RhoA and Rac during CE (Tahinci and Symes, 2003), a re-examination using mosaic labeling should be highly informative. Thus, our work here provides not only insights but also tools for a deeper understanding of *Xenopus* CE specifically and the mechanisms integrating biomechanical forces that drive animal morphogenesis generally.

Limitations of the study

Unlike more-studied epithelial cells in CE, which have a clear apicobasal polarity, these mesenchymal cells are spindle-shaped along the mediolateral axis. The radial shape symmetry allowed us to look into different cellular mechanisms and their interaction only

at the focal plane where cell-cell interface is vertical to focal plane and is sharp under the scope. However, our recent work has revealed a differential adhesion network between the superficial cell-extracellular matrix (ECM) interface and the deeper cell-cell interface (Huebner et al., 2022). Thus, the adhesion-dependent cell crawling and its integration with the cortical contraction may have a different pattern at the superficial cell-ECM interface. It is likely to skew the cell intercalation pattern shown in Figures 2F and S4C. For the pair comparison of our *in vivo* and *in silico* results, we also did not consider the cell behaviors at the cell-ECM interface.

STAR★METHODS

RESOURCE AVAILABILITY

Lead contact—Further information and requests for resources and reagents should be directed to and will be fulfilled by the lead contact, John B. Wallingford (wallingford@austin.utexas.edu).

Materials availability—This study did not generate new unique reagents.

Data and code availability

- All data reported in this paper will be shared by the lead contact upon request.
- All original code has been deposited at Mendeley Data and is publicly available as of the date of publication. DOIs are listed in the key resources table.
- Any additional information required to reanalyze the data reported in this paper is available from the lead contact upon request.

EXPERIMENTAL MODEL AND SUBJECT DETAILS

Animals

***Xenopus laevis*:** *Xenopus laevis* adult male and female frogs were obtained from Nasco (LM00531MX and LM00713M) and *Xenopus* 1(4290 and 4270) and maintained according to standard procedures. All work was carried out following the University of Texas at Austin, Institutional Animal Care and Use Committee (IACUC) protocols #AUP-2018-00,225 and #AUP-2021-00,167.

METHOD DETAILS

***Xenopus* embryo manipulations**—Ovulation was induced by injecting adult female *Xenopus laevis* with 600 units of human chorionic gonadotropin (HCG, MERCK Animal Health) and animals were kept at 16 dc overnight. Eggs were acquired the following day by squeezing the ovulating females and eggs were fertilized *in vitro*. Eggs were dejellied in 2.5% cysteine (pH 7.9) 1.5 h after fertilization and reared in 1/3× Marc's modified Ringer's (MMR) solution. For micro-injection, embryos were placed in 2% ficoll (Fisher Scientific) in 1/3× MMR during injection and washed in 1/3× MMR 30 min after injection. Embryos were injected in the dorsal blastomeres at the 4-cell stage targeting the C1 cell at 32-cell stage and presumptive notochord. Keller explants were dissected at stage 10.25 in Steinberg's solution using hair tools and cultured until stage 14 for imaging.

mRNA and morpholino microinjections—Capped mRNAs were generated using the ThermoFisher SP6 mMessage mMachine kit (Catalog number: AM1340). mRNAs were injected at the following concentrations per blastomere: Mem-BFP (75 pg), Lifeact-RFP (75 pg), and Lifeact-GFP (75 pg). Arvcf morpholino was injected at a concentration of 30 ng per blastomere.

Imaging *Xenopus* explants—Explants were submerged in Steinberg's solutions and cultured on glass coverslips coated with Fibronectin (Sigma-Aldrich, F1141) at 5 $\mu\text{g}/\text{cm}^2$. After 5-h incubation at room temperature, we started standard confocal time-lapse imaging using a Nikon A1R. Images of membrane-BFP, Lifeact-GFP, and Lifeact-RFP were taken at a focal plane 5 μm deep into the explant and at an interval of 10 s.

Cell segmentation—All image process and analysis were performed using customized MATLAB scripts if not mentioned otherwise. We first performed cell segmentation and junction detection on images of Membrane-BFP. Briefly, we used pixel classification in ilastik (Berg et al., 2019), a machine-learning based open-resource image analysis tool, to classify pixels at cell-cell interface and pixels in cytoplasm. This process converted a time-lapse movie of fluorescence intensity images to a time-lapse movie of probability images for cell-cell interface. We then extracted skeletons where the probability peaks at each time point for a robust detection of cell-cell interfaces and cell segmentation.

Kymograph preparation—We customized the preparation of kymograph so that it not only displays actin fluorescence intensity values from crawling (ML cells) or contraction (AP cells) signals but also displays the movement of tricellular vertices explicitly. Briefly, we extracted 2 μm thick bands along the AP cell interface from images of actin labeling, linearized the bands, calculated the normalized mean fluorescence intensity across the thickness, then stacked data from each time point along the time axis. For a direct display of tricellular vertex movement, we used in-plane displacement at each time point, defined in Figure S2A, as a reference to align the kymograph.

Measurement of cell intercalation—We defined cell intercalation as the displacement of a tricellular vertex along the direction to shorten the AP interface (Figure S2A). Each tricellular vertex was tracked over time on the segmented images and its displacement in the tangential direction of the AP interface (“in-plane”) between adjacent timepoints was quantified (Figure S2A). The in-plane displacement is the only component that contributes to cell intercalation and junction shortening. The transverse movement of a tricellular vertex causes junction rotation and was neglected here. To keep it simple, the in-plane displacement is referred to as “vertex displacement”, “intercalation displacement”, or “displacement”. We quantified cell intercalation at each tCR separately because their behaviors were independent (Figure S3A).

Measurement of actin dynamics for crawling and contraction—For the quantification of actin intensity associated with crawling or contraction, a 2 μm thick band along the AP cell interface was extracted from the fluorescent image of actin for ML cells or AP cells respectively (Figures S2D and S2E). For each time point, we divided such bands into tricellular regions (tCRs) and the middle region (Mid) for the analysis of

regional actin dynamics. The tCRs have a minimum length of 4 μm at any time point and covered the entire protrusions from the ML cells if there were any. The middle regions were complementary to the tCRs and had a minimum length of 2 μm (Figure S2E). The raw crawling and contraction signals for cell intercalation were the mean actin fluorescence intensity in the correspondence tCRs or the middle region as specified (Figure S2G). The necessity for such a regional analysis is apparent, since actin dynamics are highly heterogeneous long the AP interface (Figures 1L and 1M). The low correlation between the contraction signal in a tCR and that in the adjacent middle region also supports this regional analysis (Figure S3F). Since contraction from the middle region of a junction has minor contribution to cell intercalation (Figure S4C), this manuscript focuses on actin dynamics in tCRs and contraction signals refer to contraction in tCRs if not otherwise specified.

Normalization of fluorescence intensity signals—To allow for comparison of fluorescence intensity from different cells and from different actin biosensors, we normalized the fluorescence intensity of each cell with its mean cytosolic background intensity. Briefly, we used cell segmentation mentioned earlier to generate a cytosolic mask for each cell which excluded cell-cell interface and cell cortex with a 3 μm margin (Figure S2C). The mean fluorescence intensity within each cytosolic mask was quantified and its moving average over 6 min was calculated and used for normalization (Figures S2F–S2H).

Intercalation step analysis by correlating actin dynamics and cell movement

—To understand the underlying mechanisms for cell intercalation, we first performed cross-correlational analysis between the intercalation velocity traces and the traces of actin dynamics for crawling or contraction (Figures S3C–S3D). Vertex velocity traces were chosen rather than the vertex displacement for the dynamics of cell intercalation, because displacement is the integral of a velocity and trails the dynamics of the velocity (Figure S2B). The bulk analysis shown low cross correlation between the cell movement and actin dynamics (Figures S3C–S3D), suggesting a more complex mode of cell intercalation than crawling or contraction alone. Meanwhile, the contraction signals and crawling signals in tCRs were better correlated in over half of the cases (Figure S3E), suggesting an active integration between them.

To infer the driving force for cell intercalation at a finer temporal resolution, we took the advantage of the pulsatile nature of both actin dynamics and cell movement during CE. We first identified peaks in the intercalation velocity curves as single intercalation “steps”, then searched for cross-correlated peaks in the crawling and contraction signals from tCRs within a 40-s window preceding the velocity peak (Figure 2A; e.g. Figure S4A; threshold for cross-correlation: 0.5). If an intercalation step is correlated with a peak in the crawling or contraction signal, it is categorized as a crawling or contraction intercalation step (Figures 2B and 2C). If an intercalation step is correlated with a pair of contraction and crawling peaks, it is categorized as a concurrent intercalation step (Figures 2D and 2E). Within the 40-s window, we observed comparable number of cases when a crawling peak precedes a contraction peak (Figure 2D) and cases when a contraction peak precedes a crawling peak (Figure 2E). Besides the crawling, contraction, and concurrent intercalation steps, which are the major players, we also observed intercalation steps that are correlated with

contraction peaks from the middle region of an AP interface (Figure S4B). Compare with actin dynamics in tCRs, contraction in the middle region has much less contribution to cell intercalation (Figure S4C). See also Video S3.

Vertex model to simulate convergent extension—To study how crawling and contraction act in concert to drive convergent extension, we designed a cell-based CE model that offers a detailed description of subcellular behaviors and allows for cells taking an arbitrary shape under subcellular forces. The design of the model is inspired by a cell-based model for the gastrulation of *Nematostella vectensis* (Tamulonis et al., 2011). Each cell is initially a hexagon and is represented by a 90-vertex polygon (Figure 5A). Interfaces between any neighboring cells are allowed to connect via cell-cell adhesion (Figures 5B and 5C).

The dynamics of the model is driven by simple Newtonian mechanics with the basic assumptions: (1) vertices are embedded in viscous medium that applies a viscous dragging force with the damping parameter η and (2) inertia vanishes. This leads to the governing equation for the evolution of the position x_i of vertex i determined by

$$\eta \frac{dx_i}{dt} = F_i,$$

where F_i is the total force acting on the vertex i . Each simulation step is run by determining the forces acting on each vertex and solving the system of first-order differential equations using two-step Adam-Bashforth method with timestep $\Delta t = 0.05$. For each cell, vertices are reset every unit time so that each segment has relatively the same length and regions with high contraction do not have vertices over-crowded.

Inspired by the experimental observations, we considered three key force components in our model: (i) pushing force on the “leading” edge simulating lamellipodia and filopodia-like protrusions (“ F_{crawl} ”, Figure 5D), (ii) contractile force on cell edges simulating contraction at cell cortex (“ $F_{contract}$ ”, Figure 5E), and (iii) adhesive force between cells simulating cadherin dependent cell adhesion (“ $F_{adhesion}$ ”, Figure 5C). Secondary force components incorporated into our model include (iv) elastic cytosolic pressure maintaining the area of a cell and (v) repulsive force between cells to avoid cell collision. Without loss of generality, this model is a dimensionless, but parameters for the key force components are estimated from experimental data, maintaining their relative values in a physiological relevant range (see Table S1).

(i) Pushing force for cell crawling and protrusion extension: We considered two force components associated with the crawling force, F_{crawl} , one for lamellipodia-like pushing on the “leading” edge and one for filopodia-like pushing at a more focused region. The “leading” edge forms stochastically and polarity-dependently (i.e., randomly toward median or lateral for convergent extension). Small pushing forces with a cosinusoidal profile and the maximum magnitude of F_1 are applied on vertices along the leading edge for a period of T_f . The cosinusoidal force profile is initially centered around the anteroposterior center of the cell and could be shifted toward a protrusion when one forms as described below.

Filopodia-like protrusions form stochastically on vertices in the tricellular regions on the “leading” edges. When a protrusion site is identified, a quartile-sine force pulse with the magnitude of F_p and the duration of T_p is applied to the vertex in the direction toward the interface between its two neighboring cells (Figures S5A and S5B). For the analysis of different intercalation types, we simulated the shortening of AP interfaces exclusively and set the filopodial protrusions forming at defined time points (Figure 5H), so that we can distinguish crawling-only intercalation events from concurrent events.

(ii) Contraction at cell cortex: Contraction at cell cortex is modeled as pieces of Hill’s muscle connected in series. The contractile force between two neighboring vertices equals:

$$F_{contract} = \begin{cases} M \cdot f_{stall} \cdot (1 + \dot{\epsilon}/\dot{\epsilon}_0), & \dot{\epsilon} < 0 \\ M \cdot f_{stall} \cdot \left[1 + 0.5 \cdot \left(1 - e^{-\dot{\epsilon}/0.5 \cdot \dot{\epsilon}_0}\right)\right], & \dot{\epsilon} \geq 0 \end{cases}$$

where M is the density of actomyosin, f_{stall} is the stall force, $\dot{\epsilon}$ is the strain rate in each segment defined by adjacent vertices, and $\dot{\epsilon}_0$ is the maximum contractile strain rate when force vanishes. To mimic actomyosin pulses long the AP interface (Figure 1M), M is composed of a polarity-dependent baseline of actomyosin M_{base} , plus extra half-sine pulses M_{pulse} in the tricellular regions and/or the middle of the AP interface for a period of T_m (Figures S5A and S5B). The extra actomyosin pulses form stochastically in the 4-cell or 27-cell models. However, for the analysis of different intercalation types, we simulated the shortening of AP interfaces exclusively and set the actomyosin pulses at defined time points in tCRs only (Figure 5H), so that we can distinguish contraction-only intercalation events from concurrent events.

(iii) Cell-cell adhesion and force transmission: Cell-cell adhesion is based on cadherin clustering via its trans- and cis-interaction, and depends on force transmission via cadherin clusters and cadherin-catenin complex binding to the actomyosin network (Lecuit and Yap, 2015). We simplified cell adhesion as adhesion clusters of the size of $N_{adhesion}$ binding cell edges of adjacent cells, while holding an adhesive force of $F_{adhesion}$ (Figure 5C). The dynamics of adhesion clustering and the adhesion force are interdependent and we used a catch-bond model for the simulation (Rakshit et al., 2012; Buckley et al., 2014; Novikova and Storm, 2013).

Briefly, the force dependent unbinding rate for a single catch-bond can be expressed as $k_u(f) = k_0 \cdot [\exp(-f/f^* + \phi_c) + \exp(-f/f^* + \phi_s)]$ where k_0 is a reference unbinding rate and set to 1 s^{-1} , f is the force on the bond, f^* is a force scale used to non-dimensionalize all forces, and ϕ_c and ϕ_s represent zero-force unbinding rates associated with the catch and slip portion of the bond dynamics, respectively. Considering an adhesion cluster of the size $N_{adhesion}$ and a tensile load $F_{adhesion}$ uniformly distributed on all bonds, the temporal evolution of the cluster size is expressed as

$$\frac{dN_{adhesion}}{dt} = \gamma \cdot k_0 \cdot (N_{adhesion}^{tot} - N_{dhesion}) - k_0 \cdot \left[\exp\left(-\frac{F_{adhesion}}{N_{adhesion} \cdot f^*} + \phi_c\right) + \exp\left(\frac{F_{adhesion}}{N_{adhesion} \cdot f^*} - \phi_s\right) \right]$$

where γ is a dimensionless rebinding rate and $N_{adhesion}^{tot}$ is the polarity-dependent total adhesion units available in the vicinity. Under a quasistatic state, $N_{adhesion}$ and $F_{adhesion}$ can reach their maximum given by $N_{adhesion_max}^{tot} = \frac{\alpha\gamma}{\alpha\gamma + 2} N_{adhesion}^{tot}$ and $F_{adhesion_max} = N_{adhesion_max} \cdot \phi_{max} \cdot f^*$, where $\alpha = \exp(\phi_s/2 - \phi_c/2)$ and $\phi_{max} = (\phi_s + \phi_c)/2$ (see detailed deduction in Novikova and Storm, 2013).

Clustering is designed to initiate between any vertex-edge pair from two neighboring cells when the distance between them, d is larger than d_p , a repulsion limit defined later to avoid cell collision, but smaller than d_a , the adhesion limit. The two anchoring points of the cluster can move as the cell deforms and can sit anywhere on cell edges.

At the end of each iteration timestep, the adhesive force applied via an adhesion cluster is estimated by $F_{adhesion_e} = k_a \cdot N_{adhesion} \cdot (d - d_p)$, where k_a is the spring constant for a bond unit. k_a is estimated assuming a cluster under a slowly increasing tension reaches its maximum size of $N_{adhesion_max}$ and maximum load of $F_{adhesion_max}$ at d_a , and it equals $k_a = \frac{F_{adhesion_max}}{f^* \phi_{max} d_a}$.

(iv) Cytosolic pressure: Cytoplasm is assumed to be linearly elastic, so the difference between the current cell area A and the rest area A_r provides a pressure on cell boundary to maintain the cell size. The cytoplasm potential energy is given by $E_c = \frac{1}{2} k_c \left(\frac{A - A_r}{A_r} \right)^2$, where k_c is the cytoplasm stiffness, and the force on each vertex i can be expressed as $F_i = \nabla_i E_c = -k_c \frac{A - A_0}{A_0} \langle y_{i-1} - y_{i+1}, x_{i+1} - x_{i-1} \rangle$.

(v) Contact repulsion: Repulsive forces are applied to any vertex-edge pair from two neighboring cells if the distance between them d is less than d_r or if the vertex is inside the neighboring cell ($d < 0$). The magnitude of this repulsive force is an exponential function of d and is given by,

$$F_r = F_{rmax} - (F_{rmax} - F_{r0}) \cdot \exp\left(\frac{d}{d_r} \ln \frac{F_{max}}{F_{max} - F_{r0}}\right),$$

where F_{r0} is the repulsion at $d = 0$, and F_{max} is the maximum repulsion if the vertex is inside a neighboring cell.

QUANTIFICATION AND STATISTICAL ANALYSIS

For intercalation analysis, 57 tricellular vertices from wildtype cells from at least 10 independent experiments and 27 tricellular vertices from Arvcf KD cells from at least 3 independent experiments are pooled. For step analysis results from four-cell models simulating shortening of AP interface (as in Figures 5H–5L, 6C–6G, 7D, S7E, and S7F), 19 independent simulations were run for each set of parameters. In boxplots, each dot represents a datapoint from a vertex. The central line is the median, the box extends vertically between the 25th and 75th the percentiles, and the whiskers extend to the lower and upper limits that do not include the outliers. For violin plots and split violin plots, each dot represents an individual intercalation step/event (as in Figures 3, 5I, 5J, 6C–6E, 7C and 7D), or an individual crawling or contraction pulse (as in Figures 4, 5K, 5L, 6F, 6G, and S6) identified from the data pool. Besides the included boxes, the violin plots also show the probability density extending from the lower limits to the upper limits that do not include the outliers. All p values are calculated using Wilcoxon Rank-Sum Test (A.K.A Mann Whitney U Test; MATLAB statistics toolbox). *p < 0.05; **p < 0.005; ***p < 0.0005; N.S., not significant.

Supplementary Material

Refer to Web version on PubMed Central for supplementary material.

ACKNOWLEDGMENTS

This work was supported by grants from the NICHD (R01HD099191; 1R21HD103882), United States. We would also acknowledge Dr. Daniel J Dickinson and Dr. Abdul Naseer Malmi-Kakkada for critical reading.

REFERENCES

- Abraham VC, Krishnamurthi V, Taylor DL, and Lanni F (1999). The actin-based nanomachine at the leading edge of migrating cells. *Biophys. J* 77, 1721–1732. [PubMed: 10465781]
- Alt S, Ganguly P, and Salbreux G (2017). Vertex models: from cell mechanics to tissue morphogenesis. *Philos. Trans. R. Soc. Lond. B Biol. Sci* 372, 20150520. [PubMed: 28348254]
- Becker SFS, Mayor R, and Kashef J (2014). Cadherin-11 mediates contact inhibition of locomotion during *Xenopus* neural crest cell migration. *PLoS One* 8, e85717.
- Belmonte JM, Swat MH, and Glazier JA (2016). Filopodial-tension model of convergent-extension of tissues. *PLoS Comput. Biol* 12, e1004952. [PubMed: 27322528]
- Berg S, Kutra D, Kroeger T, Straehle CN, Kausler BX, Haubold C, Schiegg M, Ales J, Beier T, Rudy M, et al. (2019). ilastik: interactive machine learning for (bio)image analysis. *Nat. Methods* 16, 1226–1232. [PubMed: 31570887]
- Bertet C, Sulak L, and Lecuit T (2004). Myosin-dependent junction remodelling controls planar cell intercalation and axis elongation. *Nature* 429, 667–671. [PubMed: 15190355]
- Brieher WM, and Gumbiner BM (1994). Regulation of C-cadherin function during activin induced morphogenesis of *Xenopus* animal caps. *J. Cell Biol* 126,519–527. [PubMed: 8034750]
- Brodland GW (2006). Do lamellipodia have the mechanical capacity to drive convergent extension? *Int. J. Dev. Biol* 50, 151–155. [PubMed: 16479484]
- Buckley CD, Tan J, Anderson KL, Hanein D, Volkmann N, Weis WI, Nelson WJ, and Dunn AR (2014). The minimal cadherin-catenin complex binds to actin filaments under force. *Science* 346, 1254211. [PubMed: 25359979]
- Butler MT, and Wallingford JB (2017). Planar cell polarity in development and disease. *Nat. Rev. Mol. Cell Biol* 18, 375–388. [PubMed: 28293032]

- Cavanaugh KE, Staddon M, Chmiel TA, Harmon R, Budnar S, Yap AS, Banerjee S, and Gardel ML (2022). Force-dependent intercellular adhesion strengthening underlies asymmetric adherens junction contraction. *Curr. Biol* 32, 1–15. 10.1016/j.cub.2022.03.024. [PubMed: 34699783]
- Chu CW, Masak G, Yang J, and Davidson LA (2020). From biomechanics to mechanobiology: *Xenopus* provides direct access to the physical principles that shape the embryo. *Curr. Opin. Genet. Dev* 63, 71–77. [PubMed: 32563783]
- Devitt CC, Lee C, Cox RM, Papoulas O, Alvarado J, Shekhar S, Marcotte EM, and Wallingford JB (2021). Twinfilin1 controls lamellipodial protrusive activity and actin turnover during vertebrate gastrulation. *J. Cell Sci* 134, jcs254011. [PubMed: 34060614]
- Fagotto F, Rohani N, Touret AS, and Li R (2013). A molecular base for cell sorting at embryonic boundaries: contact inhibition of cadherin adhesion by ephrin/Eph-dependent contractility. *Dev. Cell* 27, 72–87. [PubMed: 24094740]
- Fang X, Ji H, Kim S-W, Park J-I, Vaught TG, Anastasiadis PZ, Ciesiolka M, and Mccrea PD (2004). Vertebrate development requires ARVCF and p120 catenins and their interplay with RhoA and Rac. *J. Cell Biol* 165, 87–98. [PubMed: 15067024]
- Fernandez-Gonzalez R, Simoes Sde M, Roper JC, Eaton S, and Zallen JA (2009). Myosin II dynamics are regulated by tension in intercalating cells. *Dev. Cell* 17, 736–743. [PubMed: 19879198]
- Finegan TM, Hervieux N, Nestor-Bergmann A, Fletcher AG, Blanchard GB, and Sanson B (2019). The tricellular vertex-specific adhesion molecule Sidekick facilitates polarised cell intercalation during *Drosophila* axis extension. *PLoS Biol.* 17, e3000522. [PubMed: 31805038]
- Fletcher AG, Cooper F, and Baker RE (2017). Mechanocellular models of epithelial morphogenesis. *Philos. Trans. R. Soc. Lond. B Biol. Sci* 372, 20150519. [PubMed: 28348253]
- Huebner RJ, and Wallingford JB (2018). Coming to consensus: a unifying model emerges for convergent extension. *Dev. Cell* 46, 389–396. [PubMed: 30130529]
- Huebner RJ, Malmi-Kakkada AN, Sarikaya S, Weng S, Thirumalai D, and Wallingford JB (2021). Mechanical heterogeneity along single cell-cell junctions is driven by lateral clustering of cadherins during vertebrate axis elongation. *eLife* 10, e65390. [PubMed: 34032216]
- Huebner RJ, Weng S, Lee C, Sarikaya S, Papoulas O, Cox RM, Marcotte EM, and Wallingford JB (2022). ARVCF catenin controls force production during vertebrate convergent extension. *Dev. Cell* 57. 10.1016/j.devcel.2022.04.001.
- Irvine KD, and Wieschaus E (1994). Cell intercalation during *Drosophila* germband extension and its regulation by pair-rule segmentation genes. *Development* 120, 827–841. [PubMed: 7600960]
- Keller R, and Hardin J (1987). Cell behaviour during active cell rearrangement: evidence and speculations. *J. Cell Sci Suppl.* 8, 369–393.
- Keller R, and Sutherland A (2020). Chapter ten - convergent extension in the amphibian, *Xenopus laevis*. In *Current Topics in Developmental Biology*, Solnica-Krezel L, ed. (Academic Press).
- Keller R, and Tibbetts P (1989). Mediolateral cell intercalation in the dorsal, axial mesoderm of *Xenopus laevis*. *Dev. Biol* 131, 539–549. [PubMed: 2463948]
- Keller R, Shih J, and Sater A (1992). The cellular basis of the convergence and extension of the *Xenopus* neural plate. *Dev. Dyn* 193, 199–217. [PubMed: 1600240]
- Keller R, Davidson LA, and Shook DR (2003). How we are shaped: the biomechanics of gastrulation. *Differentiation* 71, 171–205. [PubMed: 12694202]
- Keller R (2002). Shaping the vertebrate body plan by polarized embryonic cell movements. *Science* 298, 1950–1954. [PubMed: 12471247]
- Kim HY, and Davidson LA (2011). Punctuated actin contractions during convergent extension and their permissive regulation by the non-canonical Wnt-signaling pathway. *J. Cell Sci* 124, 635–646. [PubMed: 21266466]
- Lecuit T, and Yap AS (2015). E-cadherin junctions as active mechanical integrators in tissue dynamics. *Nat. Cell Biol* 17, 533–539. [PubMed: 25925582]
- Lienkamp SS, Liu K, Karner CM, Carroll TJ, Ronneberger O, Wallingford JB, and Walz G (2012). Vertebrate kidney tubules elongate using a planar cell polarity-dependent, rosette-based mechanism of convergent extension. *Nat. Genet* 44, 1382–1387. [PubMed: 23143599]
- Martin AC, Gelbart M, Fernandez-Gonzalez R, Kaschube M, and Wieschaus EF (2010). Integration of contractile forces during tissue invagination. *J. Cell Biol* 188, 735–749. [PubMed: 20194639]

- Merkel M, and Manning ML (2017). Using cell deformation and motion to predict forces and collective behavior in morphogenesis. *Semin. Cell Dev. Biol* 67, 161–169. [PubMed: 27496334]
- Miao H, and Blankenship JT (2020). The pulse of morphogenesis: actomyosin dynamics and regulation in Epithelia. *Development* 147, dev186502. [PubMed: 32878903]
- Mitrossilis D, Fouchard J, Guirouy A, Desprat N, Rodriguez N, Fabry B, and Asnacios A (2009). Single-cell response to stiffness exhibits muscle-like behavior. *Proc. Natl. Acad. Sci. U S A* 106, 18243–18248. [PubMed: 19805036]
- Nishimura T, Honda H, and Takeichi M (2012). Planar cell polarity links axes of spatial dynamics in neural-tube closure. *Cell* 149, 1084–1097. [PubMed: 22632972]
- Novikova EA, and Storm C (2013). Contractile fibers and catch-bond clusters: a biological force sensor? *Biophys. J* 105, 1336–1345. [PubMed: 24047984]
- Paulson AF, Mooney E, Fang X, Ji H, and Mccrea PD (2000). Xarvcf, Xenopus member of the p120 catenin subfamily associating with cadherin juxtamembrane region*. *J. Biol. Chem* 275, 30124–30131. [PubMed: 10899158]
- Petrie RJ, Koo H, and Yamada KM (2014). Generation of compartmentalized pressure by a nuclear piston governs cell motility in a 3D matrix. *Science* 345, 1062. [PubMed: 25170155]
- Pfister K, Shook DR, Chang C, Keller R, and Skoglund P (2016). Molecular model for force production and transmission during vertebrate gastrulation. *Development* 143, 715–727. [PubMed: 26884399]
- Prass M, Jacobson K, Mogilner A, and Radmacher M (2006). Direct measurement of the lamellipodial protrusive force in a migrating cell. *J. Cell Biol* 174, 767–772. [PubMed: 16966418]
- Rakshit S, Zhang Y, Manibog K, Shafraz O, and Sivasankar S (2012). Ideal, catch, and slip bonds in cadherin adhesion. *Proc. Natl. Acad. Sci. U S A* 109, 18815. [PubMed: 23112161]
- Shih J, and Keller R (1992). Cell motility driving mediolateral intercalation in explants of *Xenopus laevis*. *Development* 116, 901–914. [PubMed: 1295743]
- Shindo A, and Wallingford JB (2014). PCP and septins compartmentalize cortical actomyosin to direct collective cell movement. *Science* 343, 649–652. [PubMed: 24503851]
- Shindo A, Inoue Y, Kinoshita M, and Wallingford JB (2019). PCP-dependent transcellular regulation of actomyosin oscillation facilitates convergent extension of vertebrate tissue. *Dev. Biol* 446, 159–167. [PubMed: 30579764]
- Shindo A (2018). Models of convergent extension during morphogenesis. *Wiley Interdiscip. Rev. Dev. Biol* 7, e293.
- Sun Z, Amourda C, Shagirov M, Hara Y, Saunders TE, and Toyama Y (2017). Basolateral protrusion and apical contraction cooperatively drive *Drosophila* germ-band extension. *Nat. Cell Biol* 19, 375–383. [PubMed: 28346438]
- Tada M, and Heisenberg CP (2012). Convergent extension: using collective cell migration and cell intercalation to shape embryos. *Development* 139, 3897–3904. [PubMed: 23048180]
- Tahinci E, and Symes K (2003). Distinct functions of Rho and Rac are required for convergent extension during *Xenopus* gastrulation. *Dev. Biol* 259, 318–335. [PubMed: 12871704]
- Tamulonis C, Postma M, Marlow HQ, Magie CR, De Jong J, and Kaandorp J (2011). A cell-based model of *Nematostella vectensis* gastrulation including bottle cell formation, invagination and zippering. *Dev. Biol* 351, 217–228. [PubMed: 20977902]
- Truong Quang BA, Mani M, Markova O, Lecuit T, and Lenne PF (2013). Principles of E-cadherin supramolecular organization in vivo. *Curr. Biol* 23, 2197–2207. [PubMed: 24184100]
- Uyeda TQP, Iwadate Y, Umeki N, Nagasaki A, and Yumura S (2011). Stretching actin filaments within cells enhances their affinity for the myosin II motor domain. *PLoS One* 6, e26200. [PubMed: 22022566]
- Vanderleest TE, Smits CM, Xie Y, Jewett CE, Blankenship JT, and Loerke D (2018). Vertex sliding drives intercalation by radial coupling of adhesion and actomyosin networks during *Drosophila* germband extension. *eLife* 7, e34586. [PubMed: 29985789]
- Walck-Shannon E, and Hardin J (2014). Cell intercalation from top to bottom. *Nat. Rev. Mol. Cell Biol* 15, 34–48. [PubMed: 24355988]

- Wallingford JB, Niswander LA, Shaw GM, and Finnell RH (2013). The continuing challenge of understanding, preventing, and treating neural tube defects. *Science* 339, 1222002. [PubMed: 23449594]
- Williams M, Yen W, Lu X, and Sutherland A (2014). Distinct apical and basolateral mechanisms drive planar cell polarity-dependent convergent extension of the mouse neural plate. *Dev. Cell* 29, 34–46. [PubMed: 24703875]
- Wilson PA, Oster G, and Keller R (1989). Cell rearrangement and segmentation in *Xenopus*: direct observation of cultured explants. *Development* 105, 155–166. [PubMed: 2806114]
- Zaidel-Bar R, Zhenhuan G, and Luxenburg C (2015). The contractome – a systems view of actomyosin contractility in non-muscle cells. *J. Cell Sci* 128, 2209–2217. [PubMed: 26021351]
- Zallen JA, and Wieschaus E (2004). Patterned gene expression directs bipolar planar polarity in *Drosophila*. *Dev. Cell* 6, 343–355. [PubMed: 15030758]

Highlights

- Cell crawling and junction contraction work both independently and jointly for CE
- Integration of crawling and contraction produces more efficient cell movement in CE
- Integration is achieved via adhesion-dependent mechano-reciprocity
- A computation model recapitulates gross and fine scale features of CE, including integration of crawling and contraction

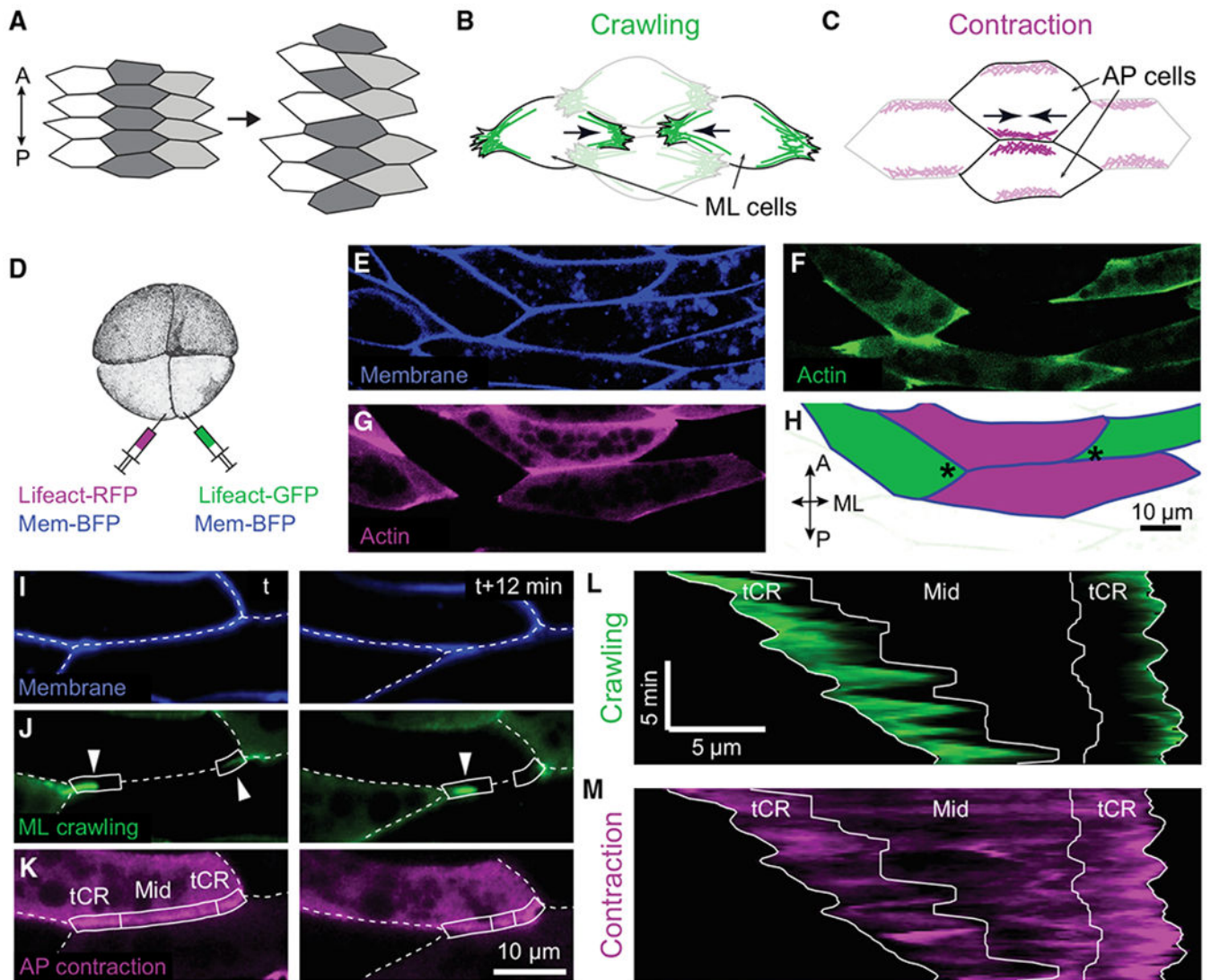


Figure 1. Mosaic labeling showing dynamics of distinct actin populations for crawling and contraction during convergent extension

(A) Illustration of convergent extension showing tissue elongation in the AP axis by cell intercalation in the orthogonal direction.

(B) Sketch showing crawling mode of convergent extension in four cells with actin in ML protrusions in green.

(C) Sketch showing contraction mode of convergent extension in four cells with actin at AP interfaces in purple.

(D) Schematic illustrating mosaic labeling technique in a *Xenopus* embryo.

(E and F) Representative images showing uniform labeling of membrane-BFP (E) and mosaic labeling of different colors of an actin biosensor (Lifeact-GFP [F] and Lifeact-RFP [G]).

(H) Example showing actin in AP cells labeled in one color and ML cells in another. Asterisks mark representative tCRs for later analysis.

(I–K) Still images from a representative time-lapse movie (Video S1, Example 1) showing membrane (I, blue), actin in the ML protrusions for crawling (J, green, arrowheads), or actin at the AP interface for contraction (K, purple). Dashed lines mark cell-cell interfaces; boxes mark tricellular regions (“tCR”) and the middle region (“Mid”); see text for details.

(L and M) Kymograph along the AP cell interface showing spatiotemporal dynamics of actin from the ML protrusions representing the “crawling” signal (L) and actin from the AP cells representing the “contraction” signal (M).

See also Figure S1 and Video S1.

Author Manuscript

Author Manuscript

Author Manuscript

Author Manuscript

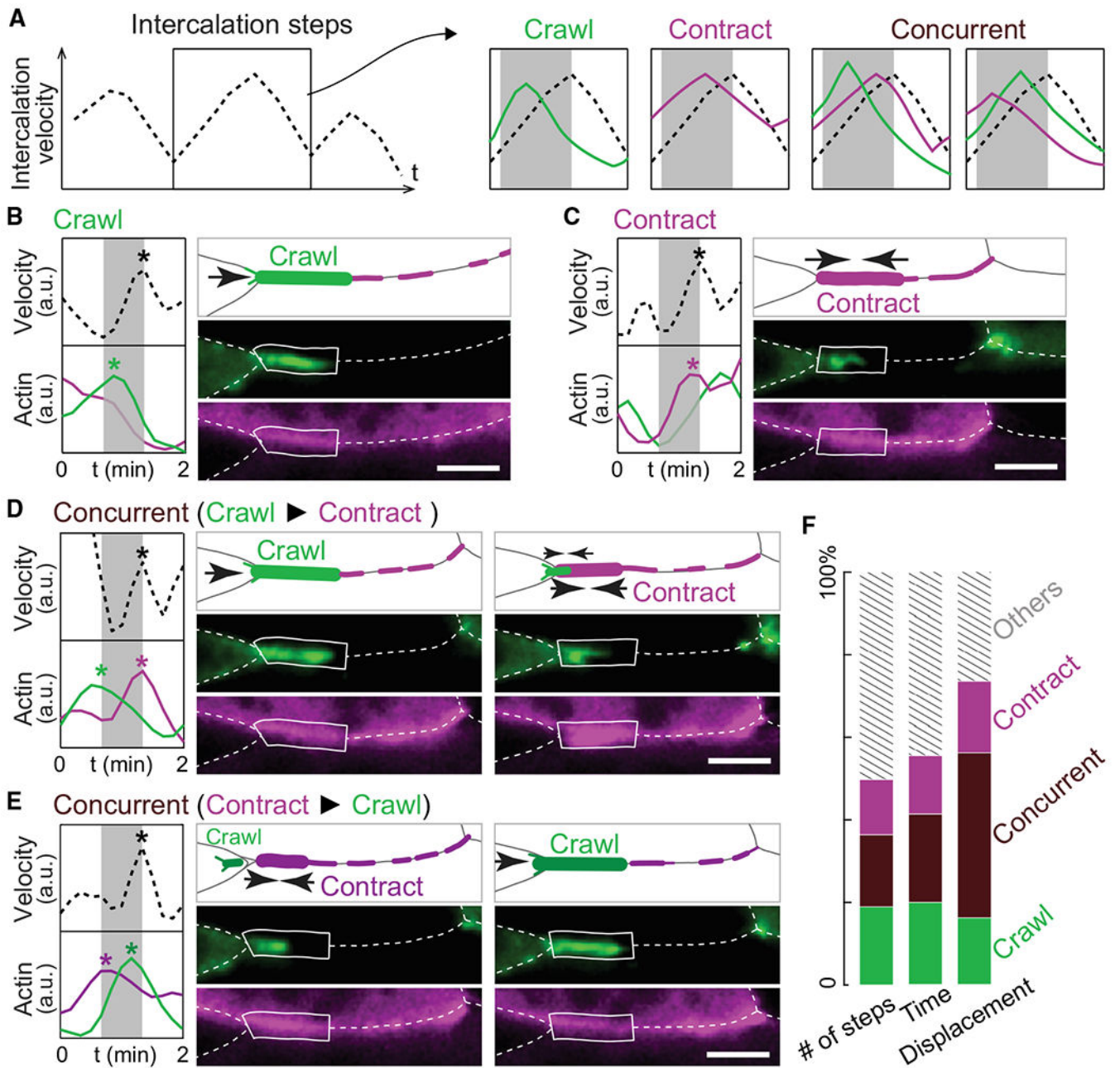


Figure 2. Direct quantification of crawling- and contraction-based cell intercalation during convergent extension

(A) Method for intercalation step analysis. Left, intercalation steps were identified as individual peaks on the trace of intercalation velocity. Right, each step is categorized based on its correlation with peaks in the crawling and/or contraction signals (green and purple, respectively). Gray boxes mark the 40-s time window for correlational analysis.

(B–E) Examples of crawling-only (B), contraction-only (C), and concurrent intercalation steps (D and E). Each shows traces of intercalation velocity and actin dynamics (left), a schematic (top-right), and still frames (bottom-right) from time-lapse data. Asterisks mark the correlated peaks of velocity, crawling, and/or contraction.

(F) Stack plots showing in percentile the number of steps, accumulative time of each step, and total displacement of cell intercalation for each category as indicated. Intercalation steps having no correlation with crawling or tCR contraction were labeled as “Others.” See also Figure S4 and Videos S2 and S3.

Author Manuscript

Author Manuscript

Author Manuscript

Author Manuscript

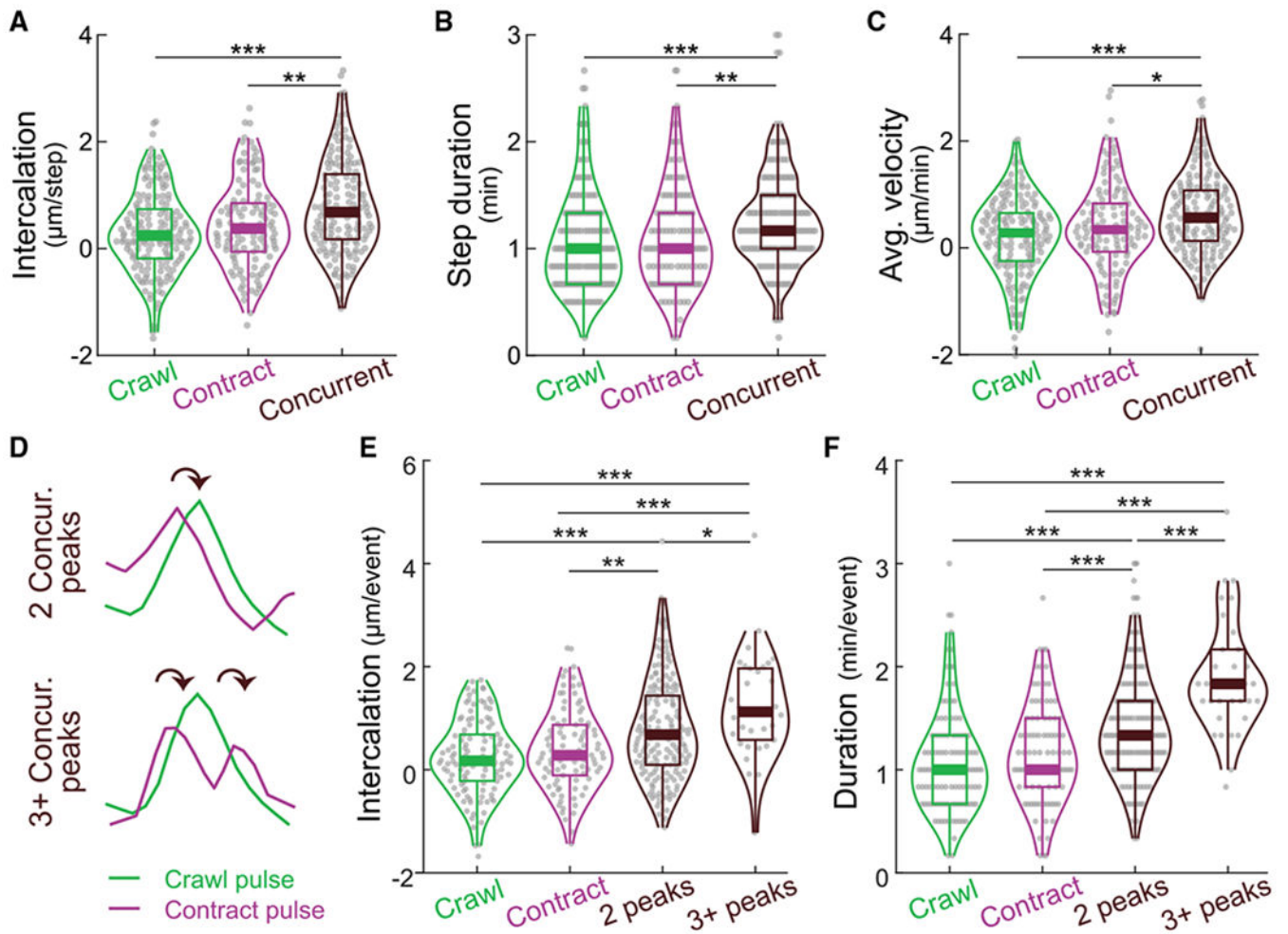


Figure 3. Concurrent crawling and contraction improve the efficacy of cell intercalation

(A) Concurrent steps produce significantly greater intercalation than do crawling or contraction steps.

(B and C) Concurrent steps increase both the step duration and average intercalation velocity.

(D) Sketch showing multiple concurrent crawling and contraction pulses (“3 + Concur. peaks”).

(E and F) Multiple concurrent crawling and contraction pulses (“3 + peaks”) further improve the intercalation displacement and duration. p values are calculated using Wilcoxon rank sum test (A.K.A. Mann-Whitney U test). * $p < 0.05$; ** $p < 0.005$; *** $p < 0.0005$; NS, not significant.

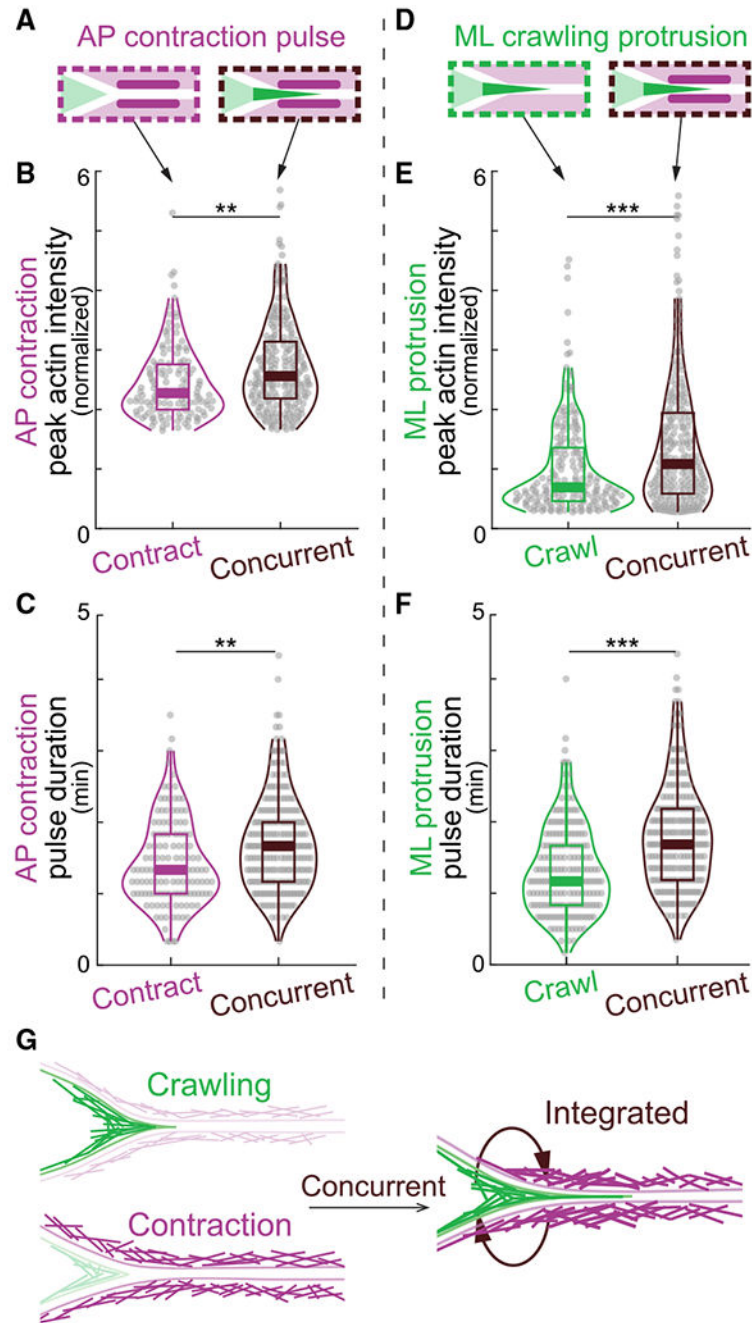


Figure 4. Integration of crawling and contraction enhances actin assembly

(A) Schematic showing contraction pulses (purple) in contraction-only and concurrent steps. (B and C) Violin plots showing increased peak actin intensity (B) and pulse duration (C) of contraction pulses when they occurred concurrently with crawling pulses compared with contraction pulses occurring alone.

(D) Schematic showing crawling protrusions (green) in crawling-only and concurrent steps.

(E and F) Increased peak actin intensity (E) and pulse duration (F) of crawling protrusions when they occurred concurrently with contraction pulses compared with crawling protrusion occurring alone.

(G) Schematic showing amplified actin assembly in crawling protrusions and contraction cortex when they are integrated during concurrent steps. p values are calculated using Wilcoxon rank sum test (A.K.A. Mann-Whitney U test). * $p < 0.05$; ** $p < 0.005$; *** $p < 0.0005$; NS, not significant.

See also Figure S4.

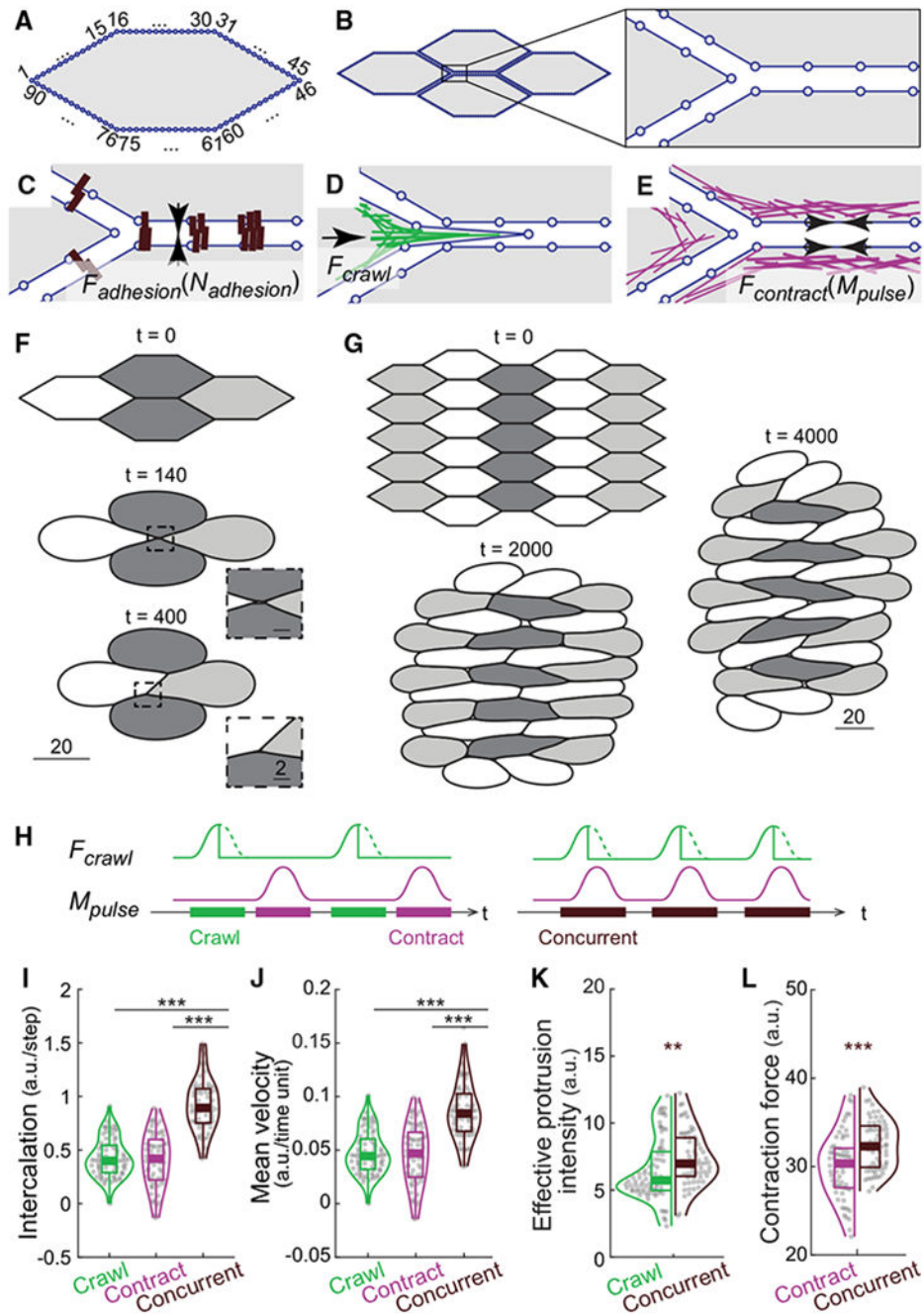


Figure 5. A vertex model provides insights into the biomechanics of crawling-contraction integration

(A) Each individual cell was modeled as a 90-vertex polygon.

(B) A four-cell model, with cell-cell interfaces modeled as independent entities.

(C–E) Schematic focused on the boxed region in (B), showing the design for subcellular modeling behaviors. (C) Cell-cell interfaces were connected via cell adhesion clusters of $N_{adhesion}$ holding adhesive forces of $F_{adhesion}$.

(D) Crawling forces F_{crawl} were applied to ML vertices around tricellular regions.

(E) Contraction forces $F_{contract}$ were added to cell cortex, which is a function of the amount of actomyosin density including the pulsatile component M_{pulse} .

(F) Representative simulation result of a four-cell model; magnification in insets reveals minimal extracellular gaps between cells.

(G) Representative simulation result of a 27-cell model, showing not only cell intercalation but also tissue-wide convergent extension.

(H) Schematic showing timepoints for crawling forces and contraction pulses, so crawling-only or contraction-only intercalations steps can be distinguished from concurrent steps.

(I and J) The model recapitulates enhanced intercalation displacement and higher velocity for concurrent steps compared with crawling or contraction alone.

(K and L) Violin plots showing synergistic effect of integration on effective protrusion intensity (K) and AP contraction force (L), recapitulating experimental observations (see Figure 4). p values are calculated using Wilcoxon rank sum test (A.K.A. Mann Whitney U test). *p < 0.05; **p < 0.005; ***p < 0.0005; NS, not significant.

See also Figures S5 and S6.

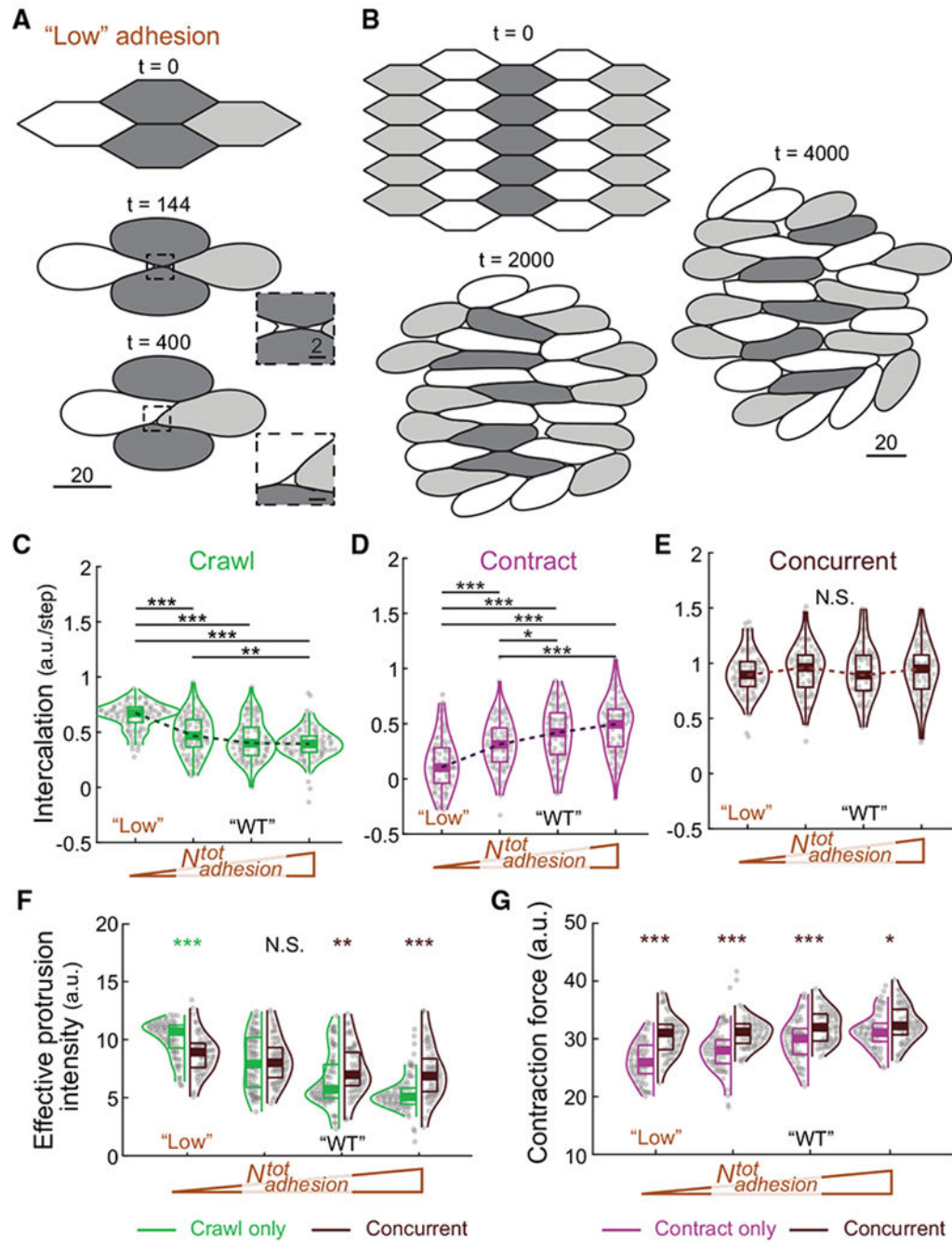


Figure 6. Role of cell adhesion in crawling and contraction

(A) Representative simulation result of a four-cell model with low adhesion showing complete cell intercalation. Magnification in insets shows enlarged voids in multi-cellular regions.

(B) Simulation result of a 27-cell model with low adhesion reduced tissue-wide convergent extension.

(C–E) Effect of increasing adhesion on intercalation (vertex displacement) during crawling-only, contraction-only, and concurrent steps in the model. “WT” marks the value used for

simulating the wild-type condition in Figure 5. “Low” marks the value used for simulating the low-adhesion condition in (A) and (B).

(F) Effect of increasing adhesion on the effective protrusion intensity in crawling-only and concurrent steps. Enhanced protrusion intensity during concurrent steps is only observed with medium-high adhesion.

(G) Effect of adhesion on contraction force in contraction-only and concurrent steps.

Contraction force during concurrent steps is robustly increased in concurrent steps. p values are calculated using Wilcoxon rank sum test (A.K.A. Mann Whitney U test). *p < 0.05; **p < 0.005; ***p < 0.0005; NS, not significant.

See also Videos S4 and S5.

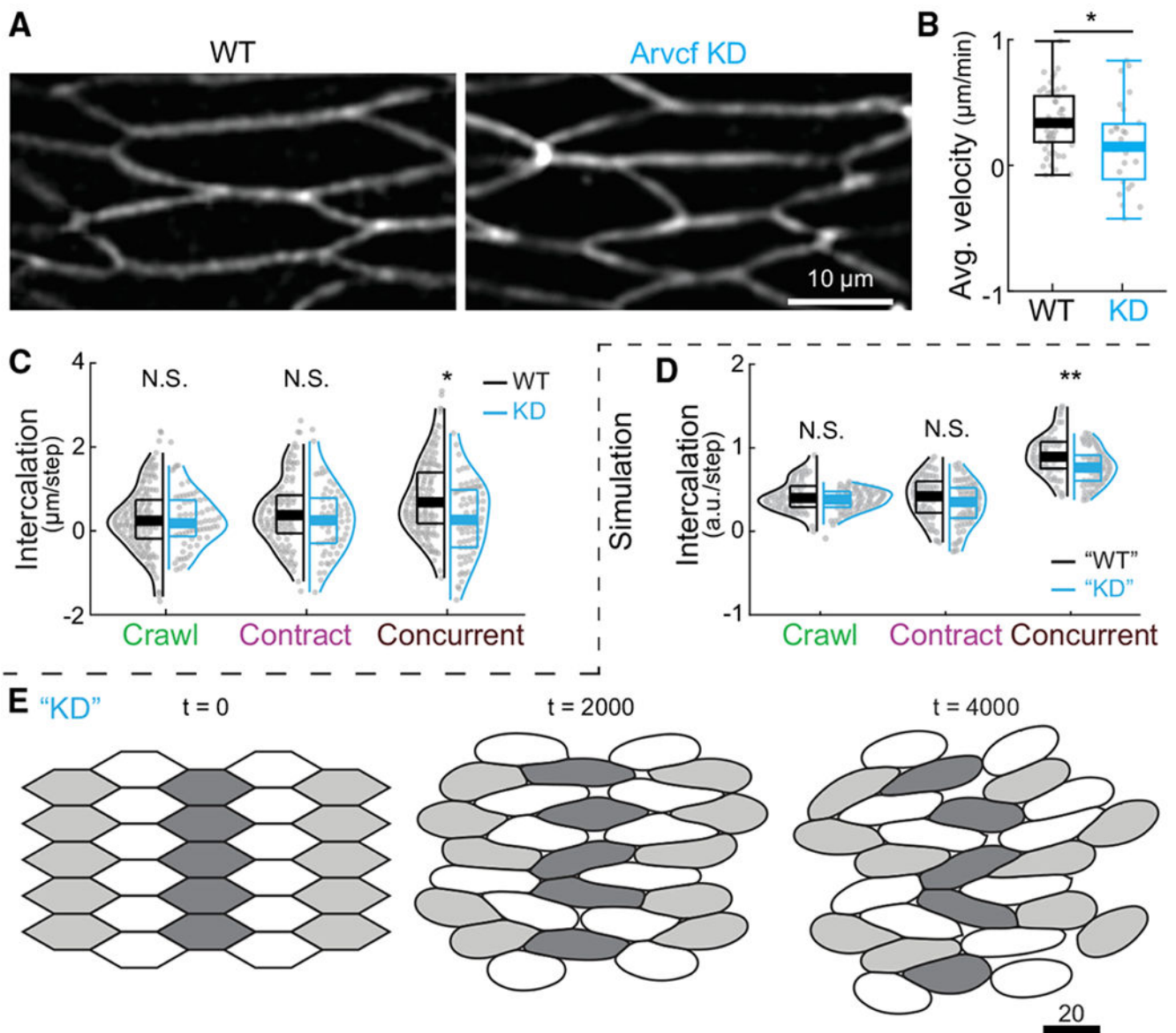


Figure 7. The Arvcf catenin is specifically required for integration of crawling and contraction (A) Still images of membrane-GFP-labeled cells showing that both wild-type and Arvcf-depleted cells were mediolaterally elongated. (B) Arvcf knockdown decreased average intercalation velocity. (C) Violin plots of intercalation (vertex displacement) in crawling-only, contraction-only, and concurrent steps. (D) Simulation results recapitulating the concurrent step-specific defect in intercalation. “KD” marks the results using a set of parameters for simulating Arvcf depletion. (E) Representative simulation result of a 27-cell model with parameters simulating Arvcf depletion. Tissue-wide convergent extension is reduced. p values are calculated using Wilcoxon rank sum test (A.K.A. Mann Whitney U test). * $p < 0.05$; ** $p < 0.005$; *** $p < 0.0005$; NS, not significant.

See also Figure S7.

Author Manuscript

Author Manuscript

Author Manuscript

Author Manuscript

KEY RESOURCES TABLE

REAGENT or RESOURCE	SOURCE	IDENTIFIER
Chemicals, peptides, and recombinant proteins		
chorulon® Human chorionic gonadotropin	MERCK Animal Health	NADA NO. 140-927; RRID:SCR_018232
Fibronectin	Sigma-Aldrich	CAT# F1141
Ficoll	Fisher Scientific	CAT# BP525
Critical commercial assays		
mMESSAGE mMACHINE™ SP6 Transcription Kit	ThermoFisher	CAT#AM1340
Experimental models: Organisms/strains		
Wild Type <i>Xenopus laevis</i> Adult Frogs	Nasco, Xenopus 1	RRID:XEP_Xla100
Oligonucleotides		
Morpholino: MMO-Arvcf 5'- ACACTGGCAGACCTGAGCCTATGGC-3'	Gene Tools (Fang et al., 2004)	N/A
Recombinant DNA		
Plasmid: Lifeact-GFP	Wallingford Lab	N/A
Plasmid: Lifeact-RFP	Wallingford Lab	N/A
Plasmid: Membrane-BFP	Wallingford Lab	N/A
Software and algorithms		
Ilastik	(Berg et al., 2019)	https://www.ilastik.org/
Matlab 2020b	https://matlab.mathworks.com/	N/A
CE models	This paper	Mendeley Data: https://doi.org/10.17632/45vmp75htk.12